

Three-dimensional model of strength and ductility of polycrystalline copper containing nanoscale twins

A. Jérusalem^a, M. Dao^b, S. Suresh^b, R. Radovitzky^{a,*}

^a Massachusetts Institute of Technology, Department of Aeronautics and Astronautics, 77 Massachusetts Avenue, Cambridge, MA 02139-4307, USA

^b Massachusetts Institute of Technology, Department of Materials Science and Engineering, 77 Massachusetts Avenue, Cambridge, MA 02139-4307, USA

Received 23 April 2008; received in revised form 14 May 2008; accepted 14 May 2008

Available online 28 June 2008

Abstract

Recent studies have shown that strength values similar to those observed in nanocrystalline metals can be obtained without a severe deterioration in ductility. This is achieved by introducing controlled, nanoscale, growth twins within ultrafine-grained metals. In this work, we present a continuum description of the effective response of nanotwinned ultrafine crystals. The model is based on a finite element formulation of the continuum three-dimensional problem. The deformation of polycrystal grains is described explicitly and the contribution of the twins is considered through a homogenized representation of the twin planes in the crystal lattice in each grain. A phenomenological three-dimensional model extending the two-dimensional model of Dao et al. [Dao M, Lu L, Shen YF, Suresh S. *Acta Mater* 2006;54:5421–32] is constructed to describe both the orientation-dependent dislocation blocking action and absorption at the twin boundaries, and its anisotropic influence on the intrinsic lattice properties. Simulations of tensile tests using this model capture the increased level of strength with increasing twin densities. The fracture initiation criterion proposed by Dao et al. is shown to provide a good description of the experimentally observed failure trends with respect to twin spacings, but to overpredict the failure strain initiation for the smallest twin spacing. Other possible failure mechanisms not considered in the model that could explain the discrepancies observed are discussed. In addition, a study of the influence of crystallographic texture on the effective response is presented. Overall, the proposed model captures the salient three-dimensional features of the deformation of nanotwinned ultrafine crystals and provides a modeling framework for predicting the transition from intragrain to intergrain mechanisms of failure.

© 2008 Acta Materialia Inc. Published by Elsevier Ltd. All rights reserved.

Keywords: Nanocrystalline materials; Nanoscale twins; Crystal plasticity; Three dimensions; Computational model

1. Introduction

Nanocrystalline metals produced by normal processing usually have a high proportion of high-angle grain boundaries [2]. The low coherence and high energy of this type of grain boundary result in residual microstrains [3]. This and the associated glass-like behavior of these grain boundaries [2] may be responsible for the low ductility of nanocrystals. With careful choice of processing conditions that minimize microstrains and promote low-angle boundaries, Lu et al.

[3] and Dao et al. [1] have shown that the ductility of nanocrystals can be significantly improved.

It is consequently of interest to design polycrystalline materials where the dislocation blocking activity of the nanocrystalline grain boundaries would remain while avoiding the low ductility associated with high-angle grain boundaries. Recent work on ultrafine crystalline copper containing nanoscale twins – a special kind of intragrain coherent boundary – has resulted in promising steps in this direction [4–6,1,7]. At such grain sizes ($d \sim 500$ nm), grain boundary deformation mechanisms are still not predominant and most of the deformation is due to intragrain dislocation-mediated plasticity [8]. Twin boundaries can then potentially act as barriers to dislocation motion, thus providing a strengthening mechanism similar to grain

* Corresponding author.

E-mail addresses: jeru@alum.mit.edu (A. Jérusalem), mingdao@mit.edu (M. Dao), ssuresh@mit.edu (S. Suresh), rapa@mit.edu (R. Radovitzky).

boundary. However, their highly coherent structure avoids the loss of ductility characteristic of nanocrystals.

Frøseth and coworkers have studied the creation and evolution of growth and deformation twins for Ni, Al and Cu using atomistic models [9–11]. The role of potential competitive mechanisms leading to the emission of partial dislocations, full dislocations or twins resulting from these studies is still a subject of debate. For Al, there is evidence that the preferred deformation mechanism when the twins are initially present is twin migration, whereas for Ni or Cu, the predominant deformation mechanism appears to be extended partial dislocation nucleation. This is explained by the much lower energy barrier for twin migration in Al – as opposed to similar energy barriers in the case of Ni and Cu – compared to dislocation emission and twin nucleation [10,11]. Asaro and Suresh [12] presented mechanistic models for the emission of partial and perfect dislocations at stress concentrations at internal interfaces and elucidated the role of intrinsic and unstable stacking fault energy in influencing deformation of nanocrystalline and nanotwinned metals. Other work by Zhu et al. emphasized the hardening effect due to the gradual loss of coherence of twin boundaries during pile-ups [13]. At the onset of plastic deformation, the undeformed twin boundary seems to favor absorption of external dislocations in the twin itself, followed eventually by a gradual loss of coherence and the accumulation of dislocations at the interface. This imbalance leads to an increase of both desorption and direct transfer between the two sides of the twin until a steady state is reached [13]. Even though these two mechanisms are not necessarily mutually exclusive, it is clear that further work is required to be able to assess their relative importance.

Important aspects of deformation and failure response of ultrafine crystals with embedded nanotwins have been studied in Refs. [5,6,1,7]. In these studies, the dependence of strength, ductility and strain-rate sensitivity on twin density have been investigated. A reduction in twin spacing is found to result in an increase in strain-rate sensitivity, strength and ductility.

On the basis of experimental observations, Dao et al. developed a two-dimensional computational model of nanotwinned ultrafine polycrystalline copper that aimed at capturing the macroscopic tensile stress–strain response [1]. In this approach, a crystal plasticity model for the bulk is used, in which slip, hardening and rate dependence are modified to account for the presence of twin boundaries acting as orientation-dependent dislocation barriers as well as dislocation sinks. In addition, a criterion for fracture initiation based on maximum slip per unit twin was proposed. The two-dimensional model correctly captures strengthening, rate-sensitivity and ductility increase observed with the decrease of twin spacing. In order to fully assess the quality of this model, it is desirable to incorporate kinematic mechanisms that are inherently three-dimensional. This requires the consideration of the totality of slip systems pertaining to the crystalline system in question as well as the analysis of microstructures developed in all three space dimensions. This, in

turn, requires large-scale simulations on parallel computers in order to compute the individual grain response as well as the grain interactions with sufficient accuracy.

In this paper, the modeling approach of Dao et al. [1] is extended to three dimensions. The model consists of a finite element formulation of the continuum problem describing the ultrafine polycrystal grains explicitly. Full grain boundary compatibility is assumed as results naturally from the finite element discretization since bulk deformation is the predominant deformation mechanism at such grain sizes. A crystal plasticity model is adopted for the bulk, in which the dislocation barrier action of the twinned slip systems is accounted for by modifying the critical resolved shear stress, rate dependence and hardening parameters of the slip systems piercing the twin boundaries, Section 2. A fracture criterion based on maximum slip per unit twin, as defined in Ref. [1], is adopted, Section 3. Comparisons of the stress–strain response and its dependence of twin density between simulations and experiments of Lu et al. [4] are provided in Section 4. The observed discrepancy is discussed and rationalized by consideration of possible failure mechanisms missing in the model. Finally, the numerical model is used to study the influence of the specimen texture on the macroscopic properties of the material.

2. Constitutive model for crystals with embedded twins

In this section, we describe the constitutive framework for modeling the response of the grain interiors of nanotwinned ultrafine crystals. The modeling approach is based on a constitutive framework for single-crystal plasticity which is modified to account for the presence of the twin boundaries. The constitutive framework of Cuitiño and Ortiz [14] recently modified by Kuchnicki et al. [15] is adopted. For completeness, we provide a summary the formulation.

The total deformation of a crystal is the result of two main mechanisms: dislocation motion within the active slip systems and lattice distortion. Following Lee [16], this points to a multiplicative decomposition

$$\mathbf{F} = \mathbf{F}^e \mathbf{F}^p \quad (1)$$

of the deformation gradient \mathbf{F} into a plastic part \mathbf{F}^p , which accounts for the cumulative effect of dislocation motion, and an elastic part \mathbf{F}^e , which accounts for the remaining non-plastic deformation. Following Teodosiu [17] and others [18–22], assume that \mathbf{F}^p leaves the crystal lattice not only essentially undistorted, but also unrotated. Thus, the distortion and rotation of the lattice is contained in \mathbf{F}^e . This choice of kinematics uniquely determines the decomposition (1). By virtue of (1), the deformation power per unit undeformed volume takes the form

$$\mathbf{P} : \dot{\mathbf{F}} = \bar{\mathbf{P}} : \dot{\mathbf{F}}^e + \bar{\Sigma} : \bar{\mathbf{L}}^p \quad (2)$$

where

$$\bar{\mathbf{P}} = \mathbf{P} \mathbf{F}^p \mathbf{T}, \quad \bar{\Sigma} = \mathbf{F}^e \mathbf{T} \mathbf{P} \mathbf{F}^p \mathbf{T}, \quad \bar{\mathbf{L}}^p = \dot{\mathbf{F}}^p \mathbf{F}^p \mathbf{T}^{-1} \quad (3)$$

Here, $\bar{\mathbf{P}}$ defines a first Piola–Kirchhoff stress tensor relative to the intermediate configuration $\bar{\mathcal{B}}_t$, and $\bar{\mathbf{\Sigma}}$, a stress measure conjugate to the plastic velocity gradients $\bar{\mathbf{L}}^p$ on $\bar{\mathcal{B}}_t$. The work conjugacy relations expressed in (2) suggest plastic flow rules and elastic stress–strain relations of the general form

$$\bar{\mathbf{L}}^p = \bar{\mathbf{L}}^p(\bar{\mathbf{\Sigma}}, \bar{\mathbf{Q}}), \quad \bar{\mathbf{P}} = \bar{\mathbf{P}}(\mathbf{F}^e, \bar{\mathbf{Q}}) \quad (4)$$

Here, $\bar{\mathbf{Q}}$ denotes some suitable set of internal variables defined for an intermediate configuration, for which equations of evolution, or hardening laws, are to be supplied. A standard exercise shows that the most general form of (2) consistent with the principle of material frame indifference is

$$\bar{\mathbf{P}} = \mathbf{F}^e \bar{\mathbf{S}}(\bar{\mathbf{C}}^e), \quad \bar{\mathbf{C}}^e = \mathbf{F}^{eT} \mathbf{F}^e \quad (5)$$

where $\bar{\mathbf{S}} = \bar{\mathbf{C}}^{e-1} \bar{\mathbf{\Sigma}}$ is a symmetric second Piola–Kirchhoff stress tensor relative to the intermediate configuration $\bar{\mathcal{B}}_t$, and $\bar{\mathbf{C}}^e$ is the elastic right Cauchy–Green deformation tensor on $\bar{\mathcal{B}}_t$. For most applications involving metals, a linear – but anisotropic – relation between $\bar{\mathbf{S}}$ and the elastic Lagrangian strain $\bar{\mathbf{E}}^e = (\bar{\mathbf{C}}^e - \mathbf{I})/2$ can be assumed without much loss of generality [14]. Higher-order moduli are given by Teodosiu [23].

From the kinematics of dislocation motion, it has been shown by Taylor [24] and Rice [22] that (4) is of the form

$$\bar{\mathbf{L}}^p = \sum_{\alpha} \dot{\gamma}^{\alpha} \bar{\mathbf{s}}^{\alpha} \otimes \bar{\mathbf{m}}^{\alpha} \quad (6)$$

where $\dot{\gamma}^{\alpha}$ is the shear rate on slip system α and $\bar{\mathbf{s}}^{\alpha}$ and $\bar{\mathbf{m}}^{\alpha}$ are the corresponding slip direction and slip plane normal. At this point, the assumption is commonly made that $\dot{\gamma}^{\alpha}$ depends on stress only through the corresponding resolved shear stress τ^{α} , i.e.

$$\dot{\gamma}^{\alpha} = \dot{\gamma}^{\alpha}(\tau^{\alpha}, \bar{\mathbf{Q}}) \quad (7)$$

which is an extension of Schmid’s rule. If (7) is assumed to hold, then it was shown by Rice [22] and by Mandel [21] that the flow rule (6) derives from a viscoplastic potential.

In order to complete the constitutive description of the crystal, hardening relations governing the evolution of the internal variables $\bar{\mathbf{Q}}$ need to be provided. In this work, we adopt the face-centered cubic (fcc) crystal plasticity hardening model of Cuitiño and Ortiz [14]. A synopsis of the main assumptions of the model together with the key constitutive relations is provided below for completeness. A detailed history of pioneering studies of finite crystal deformation and review of classic experimental work on crystal hardening may be found in Refs. [25,26].

The rate of shear deformation on slip system α is given by a power-law of the form:

$$\dot{\gamma}_{\alpha} = \begin{cases} \dot{\gamma}_0 \left[\left(\frac{\tau^{\alpha}}{g^{\alpha}} \right)^{1/m^{\alpha}} - 1 \right] & \text{if } \tau^{\alpha} \geq g^{\alpha}, \\ 0 & \text{otherwise.} \end{cases} \quad (8)$$

In this expression, m^{α} is the strain-rate sensitivity exponent, $\dot{\gamma}_0$ is a reference shear strain rate and g^{α} is the shear flow

stress on slip system α . Implicit in the form in which (8) is written is the convention of differentiating between the positive and negative slip directions $\pm \mathbf{m}^{\alpha}$ for each slip system, whereas the shear strain rates $\dot{\gamma}^{\alpha}$ are constrained to be non-negative.

For multiple slip, the evolution of the flow stresses is found from an analysis based on statistical mechanics to be governed by a diagonal hardening law:

$$\dot{g}^{\alpha} = \sum_{\alpha} h^{\alpha\alpha} \dot{\gamma}^{\alpha} \quad (9)$$

where $h^{\alpha\alpha}$ are the diagonal hardening moduli:

$$h^{\alpha\alpha} = \left(\frac{\tau_c^{\alpha}}{\gamma_c^{\alpha}} \right) \left(\frac{g^{\alpha}}{\tau_c^{\alpha}} \right)^3 \left\{ \cosh \left[\left(\frac{\tau_c^{\alpha}}{g^{\alpha}} \right)^2 \right] - 1 \right\} \quad (\text{no sum in } \alpha) \quad (10)$$

In this expression,

$$\tau_c^{\alpha} = r \mu b \sqrt{\pi n^{\alpha}} \quad \text{and} \quad \gamma_c^{\alpha} = \frac{b \rho^{\alpha}}{2 \sqrt{n^{\alpha}}} \quad (\text{no sum in } \alpha) \quad (11)$$

are a characteristic shear stress and strain for the slip system α , respectively. The values of τ_c^{α} and γ_c^{α} determine the location of the “bend” in the resolved shear stress–slip strain curve associated with the observable yielding during experiments. Thus, τ_c correlates well with the value of the flow stress determined by back extrapolation. In expressions (11), μ is the shear modulus, n^{α} is the density of obstacles in slip system α , ρ^{α} is the dislocation density in slip system α , b is the Burgers vector and r is a numerical coefficient of the order of 0.3 that modulates the strength of the obstacle in slip plane α given by a pair of forest dislocations separated by a distance l . This strength is estimated as

$$s^{\alpha} = r \frac{\mu b}{l} \quad (12)$$

In order to complete the constitutive formulation, evolution equations for the obstacle density n^{α} and dislocation density ρ^{α} are provided. Evidently, n^{α} is a function of the dislocation densities in all remaining systems. The experimental work of Franciosi and co-workers [27–31] is suggestive of a dependence of the form

$$n^{\alpha} = \sum_{\beta} a^{\alpha\beta} \rho^{\beta} \quad (13)$$

Experimentally determined values of the interaction matrix $a^{\alpha\beta}$ have been previously given by Franciosi and Zaoui [27] for the 12 slip systems belonging to the family of {111} planes and <110> directions in fcc crystals. They classify the interactions according to whether the dislocations belong to the same system (interaction coefficient a_0), fail to form junctions (interaction coefficient a_1), form Hirth locks (interaction coefficient a_1), co-planar junctions (interaction coefficient a_1), glissile junctions (interaction coefficient a_2), or sessile Lomer–Cottrell locks (interaction coefficient a_3), with $a_0 \leq a_1 \leq a_2 \leq a_3$. Franciosi [30] has also found the interaction coefficients to be linearly dependent on the

stacking fault energy of the crystal, the degree of anisotropy increasing with decreasing stacking fault energy.

Finally, an analytical expression for the evolution of ρ^α with the applied slip strain can be developed by considering that dislocation production is dominated by multiplication by cross glide and dislocation annihilation is proportional to the probability of having two dislocations segments of different sign but same b , in a small neighborhood of each other. The resulting expression is given by

$$\rho^\alpha = \rho_{\text{sat}} \left[1 - \left(1 - \frac{\rho_0}{\rho_{\text{sat}}} \right) e^{-\gamma^\alpha / \gamma_{\text{sat}}} \right] \quad (14)$$

where ρ_{sat} and γ_{sat} are the saturation dislocation density and saturation shear strain, which are determined by the multiplication and annihilation rates.

In this model, two differences with Dao et al.'s constitutive model arise in the definitions of the diagonal hardening coefficients $h^{\alpha\alpha}$ in Eq. (10), and of the shear deformation rate law $\dot{\gamma}_\alpha$ in Eq. (8). In Dao et al.'s model, a power hardening law is adopted [1]:

$$h^{\alpha\alpha}(\gamma_a) = \mu v_\alpha \left(1 + \frac{\mu}{\tau_0^\alpha} \gamma_a \right)^{v_\alpha - 1} \quad (15)$$

where v_α and τ_0^α are, respectively, the strain hardening exponent and the critical resolved shear stress for slip system α , γ_a is the accumulated sum of slips, and the shear deformation rate on slip system α is given by the following power-law form:

$$\dot{\gamma}_\alpha = \begin{cases} \dot{\gamma}_0 \left(\frac{\tau^\alpha}{g^\alpha} \right)^{1/m^\alpha} & \text{if } \tau^\alpha \geq 0, \\ 0 & \text{otherwise.} \end{cases} \quad (16)$$

The preceding framework for single-crystal plasticity is modified for the purpose of describing the influence of twins present in the lattice. The modifications are based on the two-dimensional model of Dao et al. [1] who consider the slip planes parallel to the twin boundaries as soft shear planes for easy glide dislocation motion. On the other hand, the remaining slip planes piercing the twin boundaries have a harder response, reflecting the fact that dislocation gliding in those planes will either have to change slip direction (if the Burger's vector is parallel to the line of intersection of the slip plane and the twin plane) or encounter the barriers provided by the twin boundaries (if the Burger's vector is not parallel). This consequently gives the material a preferred shearing direction [1]. In this model, the aggregate influence of the twin boundaries is considered in a homogeneous way through the twin density. The resolved shear stress, the hardening exponent and the rate sensitivity for the hard modes are accordingly modified as a function of twin spacing [1].

In the two-dimensional model, only three slip systems are considered in which the planes are perpendicular to the two dimensions considered and the slip directions are constrained to be in the plane. In the three-dimensional model proposed here, these restrictions are eliminated and all 12 slip systems in the fcc lattice are taken into

account. One of the four fcc slip planes is chosen as the twin plane and its three slip directions are taken as the soft modes. On the three remaining planes piercing the twin plane, a hard slip mode is assigned to all three slip directions which are assumed to account for the hardened response of both the slip systems on one side of the twin boundary and its mirror ones on the opposite side. Fig. 1 shows the soft and hard modes for a three-dimensional model of nanotwinned fcc crystal. In this schematic, (111) is chosen as the soft mode plane and the remaining three fcc slip planes host the nine hard mode slip directions.

In calculations, we adopt the soft and hard mode parameter values used in Ref. [1]. The critical resolved shear stress for the soft mode is taken as

$$g_0^{\text{soft}} = 67 \text{ MPa} \quad (17)$$

which is an estimate for polycrystalline Cu with grain size $d_{\text{grain}} \sim 500 \text{ nm}$ and effective yield stress of 200 MPa.

The dependence of the critical resolved shear stress of the hard modes g_0^{hard} on the twin spacing d_{twin} is assumed to follow a Hall–Petch relation:

$$g_0^{\text{hard}} = g_{\text{th}} \left(\frac{d_{\text{th}}}{d_{\text{twin}}} \right)^{1/2} \quad (18)$$

where d_{th} and g_{th} are the minimum twin spacing under which no pileup occurs and its corresponding shear strength, respectively. The values adopted for these parameters are:

$$\begin{cases} g_{\text{th}} = 1 \text{ GPa} \\ d_{\text{th}} = 13 \text{ nm} \end{cases} \quad (19)$$

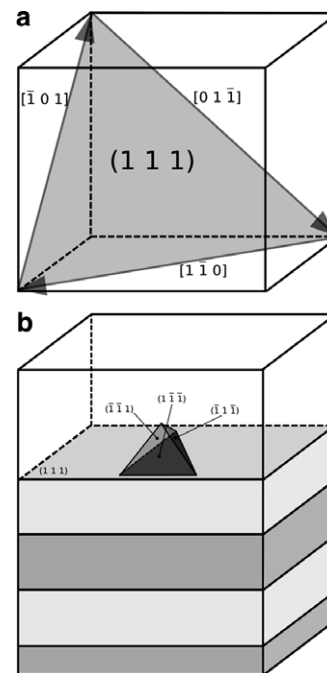


Fig. 1. Soft and hard modes for a three-dimensional model of nanotwinned fcc crystal; here, (111) is chosen as the soft mode plane and the remaining three fcc slip planes as the hard modes.

Table 1
Model parameters for Cu

C_{11} (GPa)	168.4		
C_{12} (GPa)	121.4		
C_{44} (GPa)	75.4		
$\dot{\gamma}_0$ (s^{-1})	100		
r	0.3		
b (m)	2.56×10^{-10}		
ρ_0 (m^{-2})	10^{10}		
ρ_{sat} (m^{-2})	10^{13}		
γ_{sat}	0.001		
a_0	8×10^{-4}		
a_1	40×10^{-4}		
a_2	80×10^{-4}		
a_3	120×10^{-4}		
g_0^{soft} (MPa)	67		
$h_{\alpha\beta}^{soft}$	cf. Eq. (10)		
$h_{\alpha\beta}^{hard}$	0		
d_{twin} (nm)	100	35	15
g_0^{hard} (MPa)	360.56	609.45	930.95
m	0.011	0.022	0.043

Hardening is suppressed in the hard modes by setting $h_{\alpha\beta} = 0$ in Eq. (10), reflecting the negligible strain hardening of nanocrystalline materials.

Finally, the rate sensitivity for all modes is taken as a volume-weighted average of the crystal interior sensitivity m_{XTL} and the “twin boundary affected zone” (TBAZ) sensitivity m_{TBAZ} , see Ref. [1] for detailed descriptions:

$$m_x = (1 - f_{TBAZ})m_{XTL} + f_{TBAZ}m_{TBAZ}, \quad \forall \alpha \quad (20)$$

where f_{TBAZ} is the volume fraction of the TBAZ, defined as the region around the twin boundary of thickness equal to 7–10 lattice spacings. Following Ref. [1], we take $m_{XTL} = 0.005$ and $m_{TBAZ} = 0.085$.

The full set of constants of the model for the specific case of copper considered here is given in Table 1:

3. Fracture initiation criterion

It is found experimentally that plastic deformation in nanotwinned ultrafine crystalline Cu is accompanied by dislocation pile-ups along the twin boundaries, which act

as barriers to dislocation-mediated slip on planes that are not parallel to them. Based on this observation, a failure initiation criterion was proposed in Ref. [1] which assumes that failure mechanisms become operative along twin boundaries when the slip along the twin plane reaches a threshold value δ_{max} , Fig. 2. For a given twin spacing d_{twin} , the maximum allowed shear strain in the twin systems before the initiation of failure is consequently defined by

$$\gamma_{max} = n\delta_{max} \quad (21)$$

where $n = 1/d_{twin}$ is the number of twin boundaries per unit length. It should be noted that this criterion attempts to describe local fracture initiation and not macroscopic material failure. As a result, the macroscopic strain at which failure first nucleates should be expected to be smaller than the macroscopic fracture strain, depending on the ductility of the material.

In Ref. [1], the model was calibrated against the experimental results of Lu et al. [4]. The fracture criterion was chosen such that both experimental and simulation fracture strains for $d_{twin} = 100$ nm would coincide. This was accomplished by taking $\gamma_{max} = 100\%$ for $d_{twin} = 15$ nm, which corresponds to $\delta_{max} = 15$ nm for a grain size of ~ 450 – 500 nm [1].

Using their calibrated two-dimensional model, Dao et al. studied the dependence of the tensile response on twin spacing for $d_{twin} = 100$, 35 and 15 nm, and strain rates of $6 \times 10^{-3} s^{-1}$, $6 \times 10^{-2} s^{-1}$ and $6 \times 10^{-1} s^{-1}$. The model adequately captured the deformation and failure mechanisms in nanotwinned ultrafine crystals.

Here, we investigate the suitability of this fracture criterion when three-dimensional deformation mechanisms are considered.

4. Numerical simulations

The model is evaluated by conducting simulations of the tensile stress–strain response and ductility of ultrafine copper with nanoscale twins. As part of the analysis, we investigate the dependence of the effective deformation and failure on twin density, local hydrostatic stress and initial texture distribution.

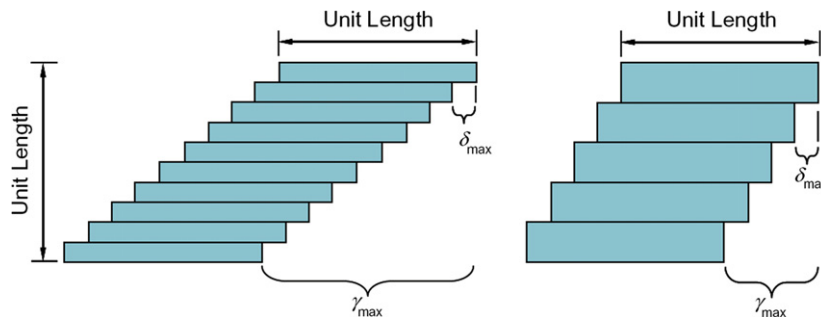


Fig. 2. Fracture criterion for twinned polycrystal adopted from Ref. [1]; each twin boundary allows a maximum slip δ_{max} , leading to a maximum shear $\gamma_{max} = n\delta_{max}$, where n is the number of twin boundaries per unit length.

4.1. Simulation setup

The model microstructure used in simulations consists of a finite element mesh of an idealized $3\ \mu\text{m} \times 3\ \mu\text{m} \times 3\ \mu\text{m}$ cube-shaped polycrystalline sample. The geometry of each grain corresponds to a tetrakaidecahedron discretized with 192 tetrahedra. The computational mesh comprises 559 500 nm size grains with a total of 82,944 tetrahedra and 15,120 interface elements, see Fig. 3.

In the experimental studies taken as the basis for model validation presented [1,6], the nanotwinned ultrafine crystal samples exhibited a crystallographic texture with twin planes predominantly perpendicular to the thin sheet surface and otherwise random crystal orientations. In our model, the (111) plane is taken as the twin plane for all grains. In agreement with the experimental observations, the initial crystal orientation for each grain is taken randomly with all twin planes constrained to remain perpendicular to one predetermined lateral facet.

For all simulations, displacement-controlled tensile test conditions are simulated by constraining the mesh nodes at the bottom face of the specimen and applying specified displacements to the nodes on the top face. The simulations are conducted on a parallel computer on 200 processors. The experimental results corresponding to a deformation rate $\dot{\epsilon} = 6 \times 10^{-4}\ \text{s}^{-1}$ are compared with the numerical results.

4.2. Simulation results

Tensile load simulations are conducted for three different twin densities corresponding to twin spacings $d_{\text{twin}} = 100, 35$ and $15\ \text{nm}$. The model parameters used in simulations are summarized in Table 1. For each twin spacing, three simulations with different crystal orientations (within the constraints described in the previous section) are conducted in order to assess the overall sensitivity of the results to the initial texture of the sample.

The stress–strain curves obtained for the three twin spacings considered are shown in Fig. 4. Instead of show-

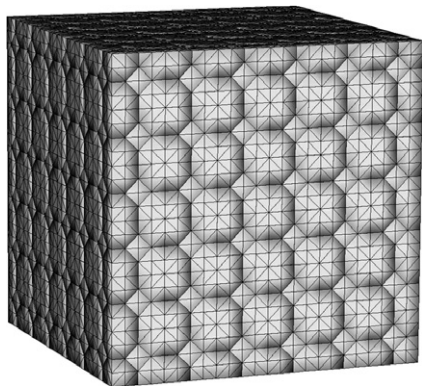


Fig. 3. Computational mesh of the nanotwinned ultrafine polycrystals used for the simulations; the dark shadows show the location of the grain boundaries.

ing the individual curves obtained for each different initial texture, the average stress–strain curve with error bars corresponding to the standard deviation is shown. These plots also show the experimental results reported in Ref. [5]. As can be observed, there is a general good agreement between experiments and simulations. In particular, the model appears to capture the dependence of the yield stress with twin spacing with reasonable accuracy.

The onset of local fracture was inferred from the simulations by monitoring the maximum slip on the twin planes. However, as explained above, this is not expected to coincide with the experimentally observed macroscopic failure. Consequently, the simulations were continued beyond the strain for which the adopted local fracture initiation criterion is satisfied, and until the macroscopic strain exceeded the corresponding experimental fracture strains.

In order to evaluate the proposed fracture criterion, we plot the evolution of the maximum slip per unit twin in the complete sample as a function of macroscopic strain, Fig. 5. The figure also shows the values of strain-to-fracture observed experimentally.

It is found that a fracture initiation criterion with a threshold value for the maximum slip of $\delta_{\text{max}} \sim 23\ \text{nm}$ matches the experimentally observed fracture for the cases where the twin spacing is $d_{\text{twin}} = 100$ and $35\ \text{nm}$. It can be interpreted that owing to the low ductility in these cases, macroscopic fracture occurs with negligible additional strain after the onset of fracture. By contrast, in the most ductile case considered, $d_{\text{twin}} = 15\ \text{nm}$, the same threshold value of the fracture initiation criterion clearly predicts a macroscopic fracture strain vastly in excess of the experimental value. Incidentally, the two-dimensional version of the model [1] fits all three failure cases using

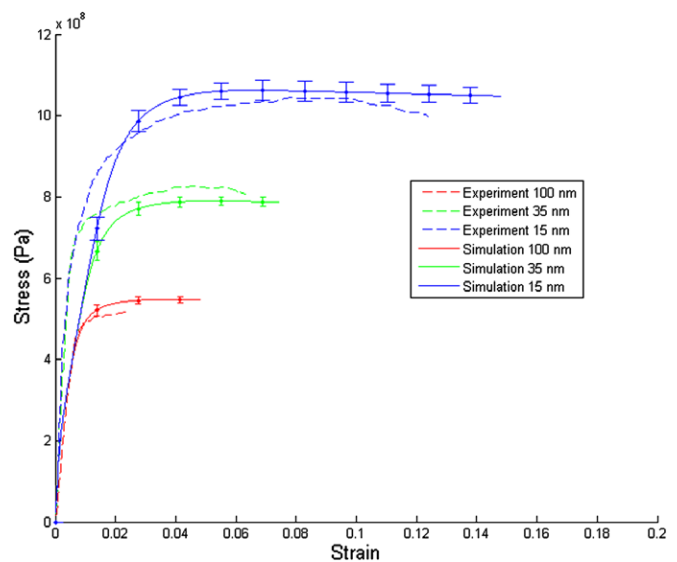


Fig. 4. Comparison of computed vs. experimental [5,6,1] tensile stress–strain response of ultrafine Cu crystals with embedded nanotwins of varying density. The values of twin spacing considered are $d_{\text{twin}} = 100, 35$ and $15\ \text{nm}$.

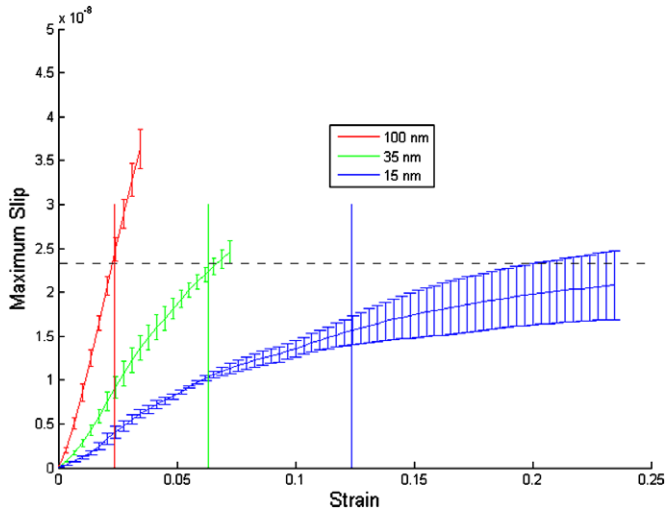


Fig. 5. Evolution of maximum computed slip per unit twin vs. strain for different twin spacings $d_{\text{twin}} = 100, 35$ and 15 nm. The crosses added to the computed curves represent the experimentally observed values of strain-to-fracture.

$\delta_{\text{max}} = 15$ nm with good accuracy. This discrepancy can probably be attributed to the intrinsic differences in the deformation mechanisms unleashed in the three-dimensional case, including out-of-plane slip, cross-slip, cross-hardening and grain rotation, which contribute to achieving the same level of macroscopic deformation with less slip in the soft modes. In turn, it is expected that these additional deformation mechanisms will activate alternative mechanisms of fracture, e.g. at grain boundaries, not considered in the simple fracture initiation model proposed.

4.3. Role of unmodeled failure mechanisms

Considering the deficiency of the proposed fracture initiation criterion in accurately capturing the dependence of failure strain on twin density across the range of densities considered, it is of interest to investigate other conceivable mechanisms at play in the failure of nanotwinned ultrafine crystals.

The simple criterion of a threshold value of the soft-mode slip is predicated on the observation that in ultrafine crystals plastic deformation is mediated by dislocation activity in the bulk of the grains. Grain boundary deformation mechanisms, e.g. sliding, only become operative for grain sizes smaller than $10\text{--}50$ nm [32]. Nevertheless, grain boundaries should be expected to play an important role in the failure of ultrafine crystals, as they usually experience stress concentrations due to strain incompatibility, which leads to void nucleation, growth, coalescence and ultimately to failure. As a consequence, a plausible cause for the discrepancy in the fracture strain obtained with the simple failure criterion proposed may be found by analyzing the role of stress concentrations at grain boundaries.

Toward this end, we analyze the case $d_{\text{twin}} = 15$ nm for which a large strain-to-fracture is observed experimentally

($\sim 12\%$) and determine whether the simulations show significant pressure (hydrostatic stress) buildup at the grain boundaries. Fig. 6 shows a snapshot of the pressure contours for the slice plane passing through the point where the pressure is maximum. Fig. 7 shows the evolution of the maximum positive and negative values of hydrostatic stress for: all points in the mesh, points at grain boundaries, triple points and grain boundary points excluding those on displacement-controlled boundaries such that the influence of boundary conditions is eliminated.

The maximum occurs at the right boundary, marked as **a** in Fig. 6. Five other local maxima above 2 GPa marked as **b** are found on this particular plane, as well as a maximum local compressive stress of approximately -2 GPa at the location marked as **c**. Note that the usual sign convention for pressure in solids is used: positive for tensile stress and negative for compressive stress. A comparison among Fig. 7a–d shows that the primary loci of hydrostatic stress maxima and minima (for tension and compression) are the intersection of grain boundaries with the displacement-controlled boundaries, followed by triple points, and grain boundaries in the interior of the sample.

The development of strong compressive stresses at grain boundaries is indicative of a bipolar hydrostatic stress distribution, which is characteristic of grain boundary incompatibilities in crystalline materials with a lamellar structure [33,34].

Fig. 8 aims at investigating the relation between the hydrostatic stress and the soft mode activity upon which the previous initiation failure criterion is based. Fig. 8a–d represent, respectively, the accumulated soft mode shear strain field, the accumulated hard mode shear strain field, the total accumulated shear strain field, and the ratio of

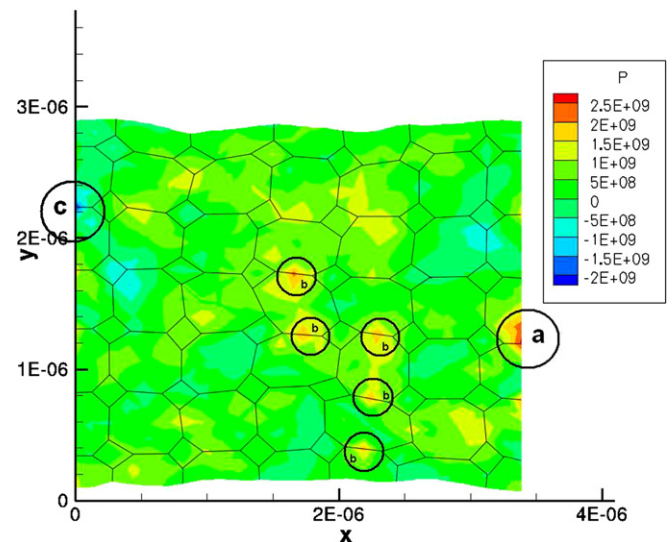


Fig. 6. Contours of hydrostatic stress for the slice plane going through the maximum; the global maximum is marked as **a**, five local maxima above 2 GPa, as **b**, and a maximum local compressive stress of approximately -2 GPa, as **c**.

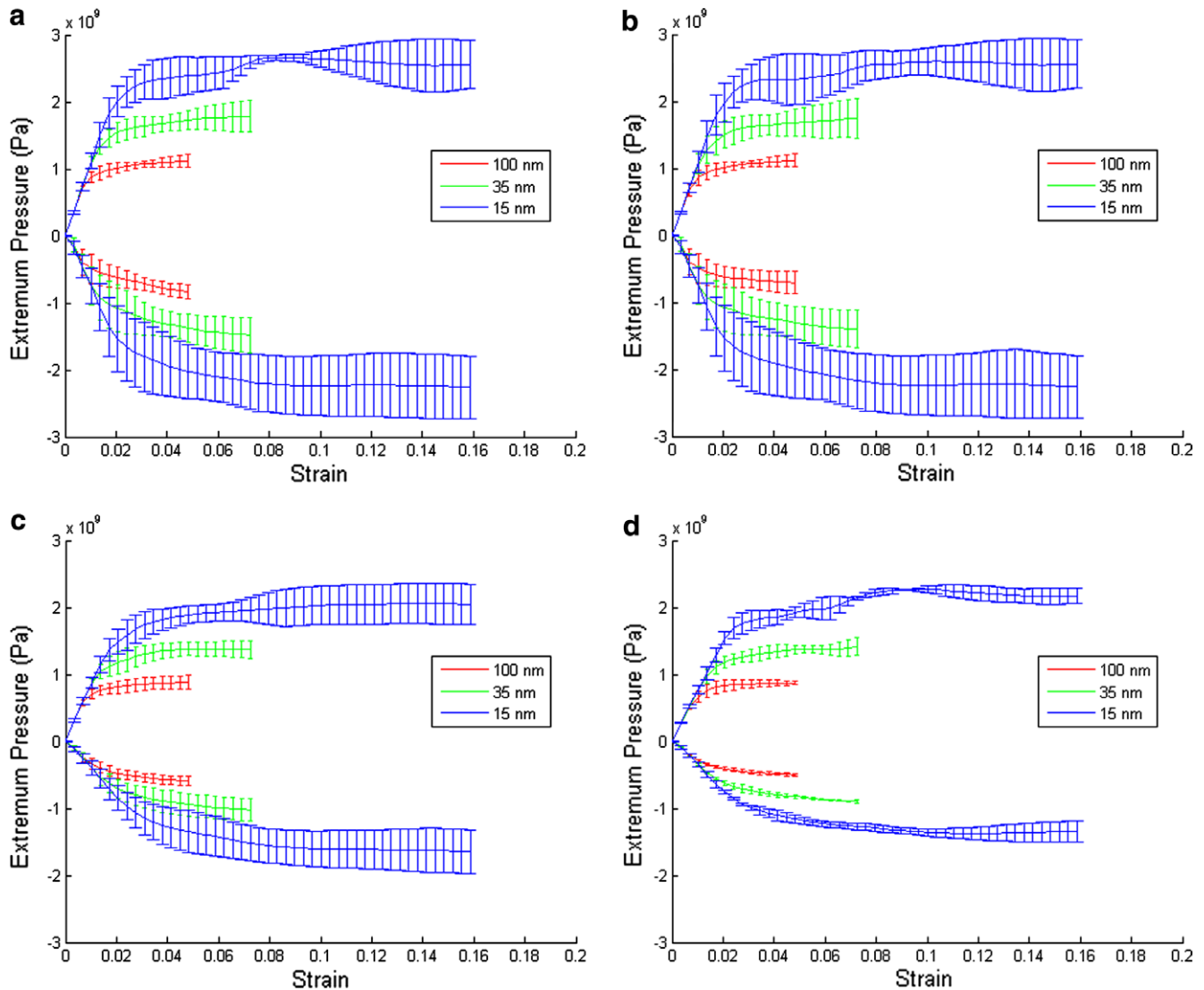


Fig. 7. Evolution of the maximum positive and negative values of hydrostatic stress for: (a) all points in the mesh, (b) points at grain boundaries, (c) triple points and (d) grain boundary points excluding intersection with displacement-controlled boundaries.

soft mode and total shear strain for the same slice shown in Fig. 6.

The comparison between Figs. 6 and 8 does not exhibit any significant correlation between the hydrostatic stress distribution, on the one hand, and either the soft or hard mode slip activity, or their relative contribution to the deformation, on the other. This observation confirms the idea that a fracture criterion based solely on soft mode activity cannot account for other mechanisms arising from hydrostatic stress concentration at grain boundaries. Based on this, we postulate the existence of a hydrostatic stress threshold above which resulting mechanisms such as void nucleation and coalescence at grain boundaries would lead to material failure. Fig. 7b implies that this threshold, if reached in the case $d_{\text{twin}} = 15$ nm, may not be reached by either of the two cases $d_{\text{twin}} = 100$ or 35 nm (this criterion is equivalent to finding the intersection of the curves with a given horizontal line on Fig. 7b). It is therefore reason-

able to conceive a change in the failure mechanism when d_{twin} decreases from 35 to 15 nm. Based on the previous observations, a twin spacing threshold can be envisioned above which the failure initiation mechanism proposed previously seems to provide a good fit, and below which a mechanism based on an hydrostatic stress threshold at grain boundaries (of the order of ~ 2.5 GPa) would apply. This criterion does not actually postulate a “switch” from one failure mode to another, but of a competition between two mechanisms where the smallest strain-to-fracture defines the dominant mechanism.

It must be emphasized that the two proposed failure mechanisms, as well as the transition from one to the other, are solely based on a limited set of experimental data. The extension of the model by Dao et al. to three dimensions nevertheless showed that a failure mechanism based exclusively on a maximum amount of slip in the soft mode cannot fully explain the experimentally observed failure.

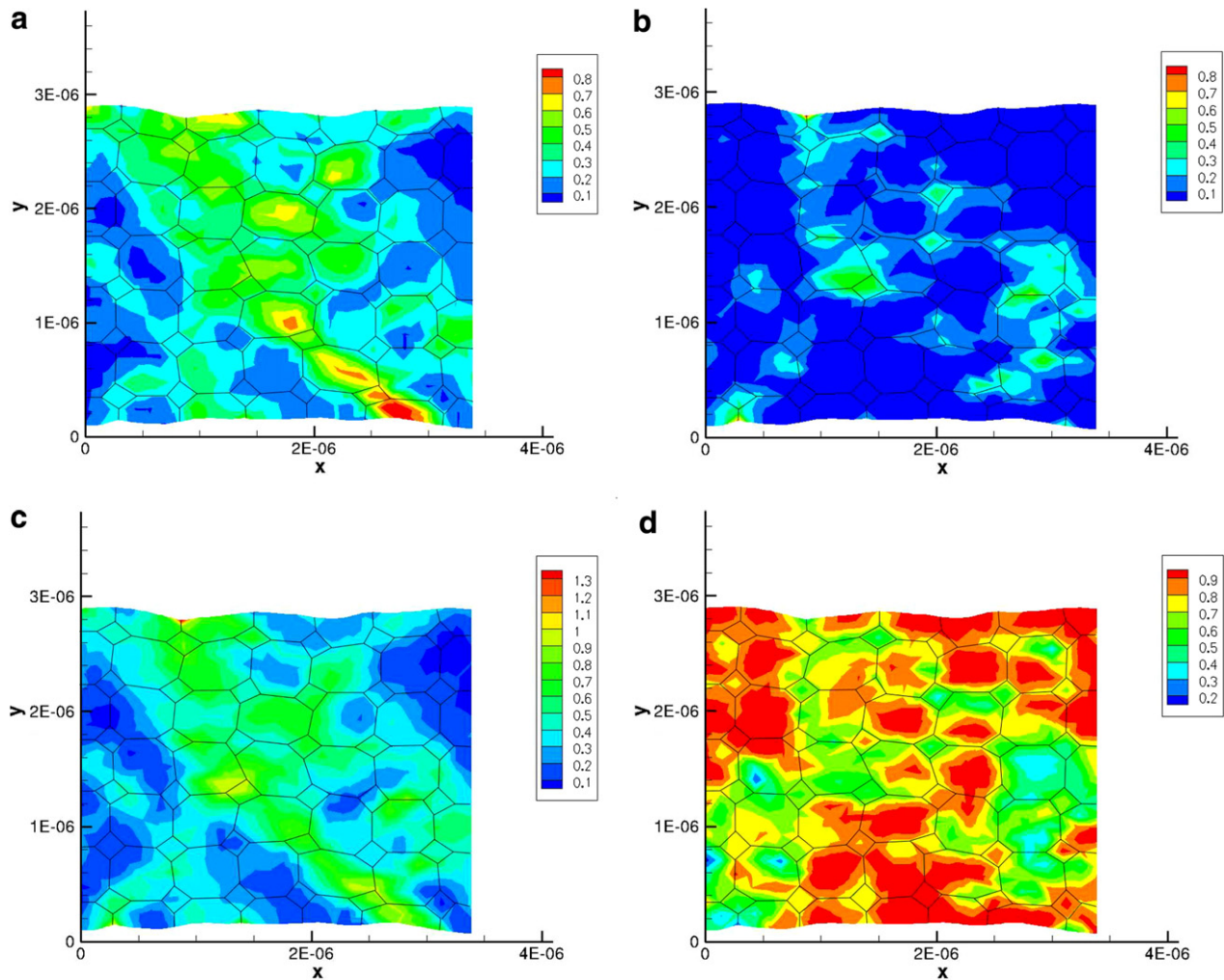


Fig. 8. (a) Represents the accumulated soft mode shear strain field, (b) the accumulated hard mode shear strain field, (c) the total accumulated shear strain field and (d) the proportion of soft mode shear strain over total shear strain; all the figures correspond to the slice of the sample at which the maximum pressure occurs.

Within these restrictions, we believe that the proposed model supports the idea of a possible hierarchy between the different key mechanisms leading to failure in nano-twinned ultrafine crystals.

4.4. Influence of initial grain orientation distribution

As mentioned above, in the as-processed material the twin planes are predominantly perpendicular to the thin sheet surface [6]. The model provides an opportunity for investigating whether more general crystallographic textures in the original material may affect the deformation and failure response. If significant, the model could guide modifications of the material processing geared at manipulating the orientation distribution functions for the purpose of further improving the effective properties of the material.

To this end, the simulations were repeated for fully random initial orientations (“non-textured case”) and compared to the results above (“textured case”). Fig. 9 shows the stress–strain curves for the two sets of simulations,

whereas Fig. 10 shows the corresponding curves of maximum and minimum hydrostatic stress and maximum slip per unit twin. On both figures, the error bars for the non-textured case are very similar to the textured case (cf. previous section) and have been omitted for clarity.

The stress–strain response, Fig. 9 remains ostensibly unaffected in the non-textured case. A similar texture-insensitive behavior can be observed in terms of the tensile hydrostatic stress, Fig. 10a and the soft mode maximum slip per unit twin, Fig. 10b. The only noticeable difference is in the maximum compressive hydrostatic stress, which grows larger than in the textured case, Fig. 10a. This indicates, in addition to a similar level of strength (cf. Fig. 9), similar strain-to-fracture values. An analysis of the hydrostatic stress contours similar to the one presented in Fig. 7 did not show any significant differences in the non-textured case.

These results suggest that further efforts to randomize the texture in the material process might not lead to significant improvements of the material properties studied in this work, namely strength and strain-to-fracture.

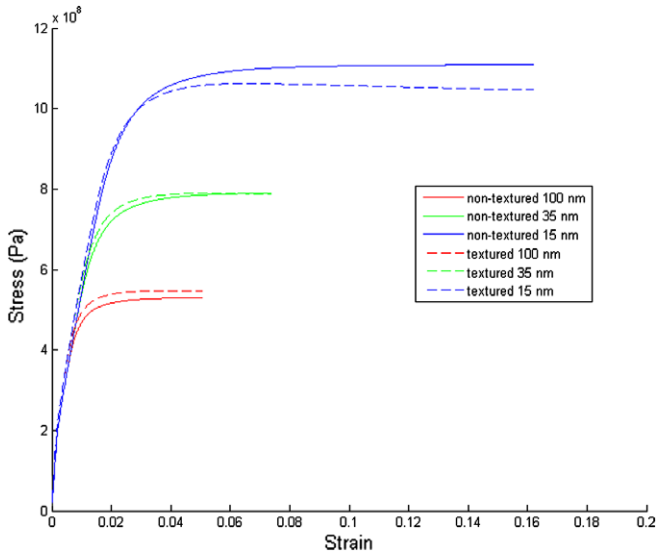


Fig. 9. Stress–strain curves for both textured and non-textured cases for different twin spacings $d_{\text{twin}} = 100, 35$ and 15 nm. Error bars for the non-textured case are very similar to the textured case and have been omitted for clarity.

5. Discussion

A three-dimensional model of ultrafine crystals with embedded growth nanotwins has been proposed. The approach is based on a crystal plasticity model for the grain bulk, modified to account for the presence of twin boundaries acting as orientation-dependent dislocation barriers as well as dislocation sinks. In addition, a failure initiation criterion consisting of a limiting value of slip on the twin planes was implemented following Ref. [1]. The consideration of out-of-plane slip, cross-slip/hardening and grain rotation enabled the investigation of three-dimensional aspects of the dependence of the stress–strain response of ultrafine copper with different nanoscale twin densities. The results showed an increase of ductility and strength with decreasing twin spacing, in agreement with experimental results, but exhibited a larger increase of strain-to-fracture initiation for the smallest twin spacings once calibrated to the largest twin spacing considered.

This suggests that additional mechanisms are available in three dimensions with respect to the two-dimensional model to accommodate the deformation, which would lead to postponed failure if only the threshold soft mode slip criterion were operative. Another failure mechanism based on hydrostatic stress concentrations at triple junctions and grain boundaries was proposed. A competition between the two mechanisms was then suggested in which for large twin spacings, tensile hydrostatic stress is low enough that a maximum slip per unit twin criterion applies (intragrain failure), whereas for small twin spacings, large hydrostatic tensile pressure at grain boundaries leads to intergrain failure.

Other possible unmodeled phenomena include the loss of coherence of twins following dislocation pileup in the

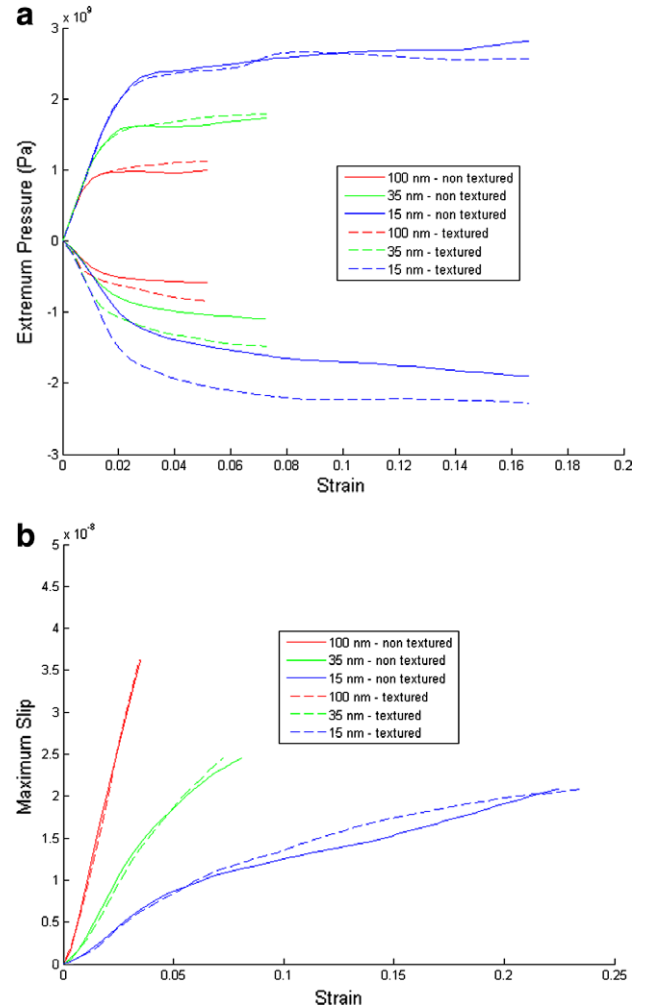


Fig. 10. Evolution of the maximum and minimum values of hydrostatic stress and maximum slip per unit twin for different twin spacings ($d_{\text{twin}} = 100, 35$ and 15 nm) in the textured and non-textured case. Error bars for the non-textured case are very similar to the textured case and have been omitted for clarity.

hard modes and the accommodation of deformation provided by the migration of twin boundaries, which has also been shown to play an important role in some cases [11]. These phenomena would lead to earlier failure and would be predominant for small twin spacings where large deformations are reached. The incorporation of these mechanisms in the model is postponed until experimental data become available providing quantitative support.

Lastly, a study of the influence of texture on deformation has shown little difference in terms of strength and failure initiation, indicating that material processing improvement efforts aiming at controlling texture may be futile.

Acknowledgements

The authors thank Prof. Lei Lu for productive discussions. R.R. and A.J. acknowledge the support of the US Department of Energy through the ASC Center for the Simulation of the Dynamic Response of Materials (DOE

W-7405-ENG-48, B523297). S.S. and M.D. acknowledge support from the Advanced Materials for Micro and Nano Systems Programme of the Singapore-MIT Alliance, as well as support from a grant to M.I.T. from the Schlumberger-Doll Company and the Office of Naval Research Grant N00014-08-1-0510 to M.I.T.

References

- [1] Dao M, Lu L, Shen YF, Suresh S. *Acta Mater* 2006;54:5421–32.
- [2] Wolf D, Yamakov V, Phillpot SR, Mukherjee A, Gleiter H. *Acta Mater* 2005;53:1–40.
- [3] Lu L, Wang LB, Ding BZ, Lu K. *J Mater Res* 2000;15:270–3.
- [4] Lu L, Shen Y, Chen X, Qian L, Lu K. *Science* 2004;304:422–6.
- [5] Lu L, Schwaiger R, Shan ZW, Dao M, Lu K, Suresh S. *Acta Mater* 2005;53:2169–79.
- [6] Shen YF, Lu L, Lu QH, Jin ZH, Lu K. *Scripta Mater* 2005;53:2169–79.
- [7] Shen YF, Lu L, Dao M, Suresh S. *Scripta Mater* 2006;55:319–22.
- [8] Dao M, Lu L, Asaro RJ, De Hosson JTM, Ma E. *Acta Mater* 2003;55:4041–65.
- [9] Frøseth A, Van Swygenhoven H, Derlet PM. *Acta Mater* 2004;52:2259–68.
- [10] Frøseth AG, Derlet PM, Van Swygenhoven H. *Appl Phys Lett* 2004;85:5863–5.
- [11] Frøseth AG, Derlet PM, Van Swygenhoven H. *Adv Eng Mater* 2005;7:16–20.
- [12] Asaro RJ, Suresh S. *Acta Mater* 2005;53:3369–82.
- [13] Zhu T, Li J, Samanta A, Kim HG, Suresh S. *Proc Natl Acad Sci* 2007;104:3031–6.
- [14] Cuitiño AM, Ortiz M. *Modell Simul Mater Sci Eng* 1992;1:255–63.
- [15] Kuchnicki S, Cuitiño A, Radovitzky R. *Int J Plast* 2006;22:1988–2011.
- [16] Lee EH. *J Appl Mech* 1969;36:1.
- [17] Teodosiu C. A dynamic theory of dislocations and its applications to the theory of the elastic–plastic continuum. In: Simmons JA, editor. *Conference of fundamental aspects of dislocation theory*, vol. 2. Washington: National Bureau of Standards Special Publication; 1969. p. 837.
- [18] Asaro R, Rice J. *J Mech Phys Solids* 1977;25:309.
- [19] Havner KS. *J Mech Phys Solids* 1973;21:383.
- [20] Hill R, Rice J. *J Mech Phys Solids* 1972;20:401.
- [21] Mandel J. *Plasticité classique et viscoplasticité*, Technical Report, Lecture Notes, International Centre for Mechanical Science, Udine. Berlin: Springer-Verlag; 1972.
- [22] Rice JR. *J Mech Phys Solids* 1971;19:433.
- [23] Teodosiu C. *Elastic models of crystal defects*. New York: Springer-Verlag; 1982.
- [24] Taylor GI. *J Inst Met* 1938;62:307–24.
- [25] Havner K. *Finite plastic deformation of crystalline solids*. Cambridge: Cambridge University Press; 1992.
- [26] Asaro RJ, Lubarda VA. *Mechanics of solids and materials*. Cambridge: Cambridge University Press; 2006.
- [27] Franciosi P, Zaoui A. *Acta Metall* 1982;30:1627–37.
- [28] Franciosi P, Zaoui A. *Acta Metall* 1983;31:1331–42.
- [29] Franciosi P. *Acta Metall* 1985;33:1601–12.
- [30] Franciosi P. Fcc single crystals hardening: anisotropy and stacking fault energy. In: *ICSMA symposium*, Montreal, Canada, 1985. p. 281.
- [31] Franciosi P. *Rev Phys Appl* 1988;23:383–94.
- [32] Kumar KS, Van Swygenhoven H, Suresh S. *Acta Mater* 2003;51:5743–74.
- [33] Kad B, Asaro DMR. *Philos Mag A* 1995;71:567–604.
- [34] Dao M, Kad B, Asaro R. *Philos Mag A* 1996;74:569–91.